PIER C

(Received 2 March 2026, Accepted 27 March 2026, Scheduled 15 April 2026)

Decoupling Control of 5-Degree-of-Freedom Permanent Magnet Assisted Bearingless Synchronous Reluctance Motor Based on Fuzzy Neural Network Inverse System

Shenshen Sui*, Yichen Liu, and Huangqiu Zhu*

School of Electrical and Information Engineering, Jiangsu University, Zhenjiang 212013, China

ABSTRACT: To achieve the dynamic decoupling of a permanent magnet-assisted bearingless synchronous reluctance motor (PMa-BSynRM), this study proposes an innovative decoupling control strategy. In this method, the inverse system is constructed by improving a genetic algorithm optimized fuzzy neural network to achieve decoupling control. Firstly, this article elucidates the structure and working principle of PMa-BSynRM, establishes a mathematical model, and conducts reversibility analysis. Secondly, by optimizing the fuzzy neural network through improved genetic algorithm, a system inverse is derived to achieve the decoupling of the initial system, transforming it into a linear-like system. Thirdly, the decoupling performance of the proposed control method for a 5-degree-of-freedom (5-DOF) system is validated through simulation. Finally, experimental validation is conducted on both 2-DOF and 3-DOF subsystems. Simulation results for the 5-DOF system and subsystem experiments indicate that the proposed method exhibits excellent control accuracy, rapid convergence, and dynamic anti-interference performance.

1. INTRODUCTION

Permanent magnet-assisted bearingless synchronous reluctance motor (PMa-BSynRM) demonstrates extensive application prospects in cutting-edge industries and high-precision, such as semiconductor manufacturing and biomedical applications, owing to its advantages of eliminating mechanical friction, requiring no lubrication, and exhibiting superior high-speed performance. The 5-degree-of-freedom (5-DOF)PMa-BSynRM integrates a 3-DOF hybrid magnetic bearing (HMB) with a 2-DOF-PMa-BSynRM configuration. By precisely controlling the rotor's position across five degrees of freedom, this motor achieves complete rotor suspension. Consequently, the research on high-performance control technologies has become imperative [1–5].

For bearingless synchronous reluctance motors, traditional decoupling methods include field-oriented control and adaptive parameter decoupling control [6], both of which are susceptible to variations in motor parameters. In strongly coupled systems, inverse system (IS) methods are commonly employed, yet existing IS-based improvements still exhibit limitations. In [7], a sliding mode variable structure (SMVS) control was used to construct an object inverse system, but this approach demonstrated weak disturbance rejection capability. In [8, 9], support vector machines (SVMs) were employed to construct the object inverse system, yet this approach remains significantly affected by parameter variations. In [10], an improved genetic algorithm optimized key parameters of the least squares support vector machine (LSSVM), effectively enhancing the decoupling performance of ORC-BPMSM systems.

Neural networks, with their exceptional nonlinear mapping capabilities, adaptive learning mechanisms, and strong robustness against complex uncertainties, have become a core technology for constructing inverse systems in various complex nonlinear systems. They are widely applied in nonlinear decoupling control and dynamic characteristic compensation. In [11], an improved genetic algorithm (IGA) was used to adjust the parameters of a back-propagation (BP) neural network, significantly enhancing both dynamic and static performance. In [12], a decoupling scheme based on BP neural networks for constructing inverse systems was proposed. To improve the dynamic response and convergence performance of neural network optimization, control algorithms integrating fuzzy inference systems with neural networks were introduced [13, 14]. Although these enhanced decoupling performance and control accuracy, they still faced the challenge of lengthy data training cycles. In [15, 16], enhanced chaos particle swarm optimization (PSO) for neural network control and an improved differential evolution (IDE) algorithm for fuzzy neural network (FNN) control were proposed, respectively. Both methods exhibit insufficient global optimization capabilities for decoupling high-dimensional complex coupled systems and limited generalization and adaptive capabilities for parameter time-varying and untrained operating conditions.

Compared to traditional methods and existing decoupling strategies, the Mamdani-type FNN demonstrates significant advantages: firstly, the fuzzy neural network architecture reduces the system's dependence on precise motion parameters. Secondly, the use of an improved genetic algorithm for FNN parameter selection during optimization not only enhances the system's adaptability but also significantly accelerates decou-

* Corresponding authors: Shenshen Sui (2222307110@stmail.ujs.edu.cn); Huangqiu Zhu (zhuhuangqiu@ujs.edu.cn).

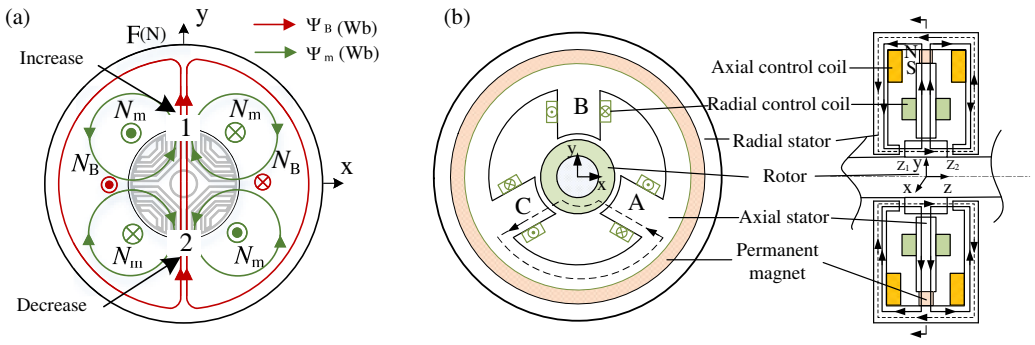

FIGURE 1. Working principle: (a) Principle of the suspension force generation; (b) Hybrid magnetic bearing circuit diagram.

pling convergence. The structure of this article is as follows. In Section 2, this paper will derive the mathematical model of PMa-BSynRM and prove its reversibility. In Section 3, the architecture of FNN and the improved genetic algorithm (IGA) optimization design are introduced. In Section 4, the simulation of the 5-DOF system is presented. In Section 5, as the 5-DOF test platform is currently being optimized, experimental validation is conducted on 2-DOF and 3-DOF subsystems to confirm the feasibility of the control method. Section 6 presents the conclusions of this study.

2. OPERATION PRINCIPLE AND MATHEMATICAL MODELING

2.1. Working Principle

The symbol annotation table is shown in Table 1. Schematic of the suspension force creation is presented in Fig. 1(a). The winding is equivalent, N_{B} is the suspension force winding and

TABLE 1. The notation table.

Variable (unit)	Physical significance
μ_0 (H/m)	Vacuum permeability
δ_0 (mm)	The air gap length when the rotor is not offset
Subscript M	Torque winding
Subscript B	Suspension winding
M (mH)	Mutual inductance
L (mH)	Self-inductance
i_0 (mA)	Equivalent magnetizing current.
m (kg)	Mass of the rotor
N	Number of turns per phase winding
θ (rad)	Rotor angular position
l_a, l_b (μm)	Distance to the center of mass
J_z (kg · mm^2)	Moment of inertia about the Z-axis
J_d (kg · mm^2)	Moment of inertia about the X and Y axes
i (mA)	The current control in different directions
x, y (μm)	Radial rotor displacement
Ψ (Wb)	Magnetic flux
k_{ir}, k_{iz} (N/A)	Current coefficient
k_{xy}, k_z (N/A)	Displacement coefficient
M_d, M_q (N/A^2)	Levitation force constants
T_{e} (N · m)	Electromagnetic torque
T_{L} (N · m)	Load torque

N_{M} is the torque winding; ψ_{B} represents the magnetic excitation in the levitation winding, and ψ_{M} represents the magnetic excitation in the torque winding. Observing Fig. 1(a) at slot 2 in the negative y-direction, ψ_{M} is opposite to ψ_{B}, weakening the magnetic field; at slot 1 in the positive y-direction, ψ_{M} is aligned with ψ_{B}, strengthening the magnetic field. This results in a radial levitation force counter to the negative y-direction. Due to this phenomenon, the radial levitation force acts along the positive y-axis direction. Consequently, by modulating both the phase and amplitude of the levitation current, the magnitude and directional orientation of the levitation force can be effectively regulated.

The structure and magnetic circuit of 3-DOF-HMB are shown in Fig. 1(b). The left section of the diagram features a dashed line representing radial control flux generated by the radial control coil, while the right section shows axial control flux from the axial control coil. Solid lines indicate the bias flux produced by permanent magnets. When the rotor deviates from radial equilibrium due to external influences, the radial control flux modifies the magnetic density between the three poles and rotor, generating radial levitation forces F_{x} and F_{y} to restore balance. Similarly, axial displacement causes the axial control flux to alter magnetic density at air-gap points Z_1 and Z_2, producing axial levitation force F_{z} that centers the rotor.

2.2. Mathematical Model of the PMa-BSynRM

The 2-DOF-PMa-BSynRM mathematical model consists of the mathematical models of two subsystems (torque subsystem and buoyancy subsystem). The Maxwell tensor method is adopted to model PMa-BSynRM [17]. The final mathematical model is as follows:

$$\begin{cases} F_d = k_{\mathrm{c}}x - (k_{\mathrm{L}} - k_{\mathrm{M}})(\psi_{\mathrm{Md}}I_{\mathrm{Bd}} + \psi_{\mathrm{Mq}}I_{\mathrm{Bq}}) \\ F_q = k_{\mathrm{c}}y - (\mp k_{\mathrm{L}} \pm k_{\mathrm{M}})(\psi_{\mathrm{Mq}}I_{\mathrm{Bd}} - \psi_{\mathrm{Md}}I_{\mathrm{Bq}}) \\ T_{\mathrm{e}} = P_{\mathrm{M}}(L_{\mathrm{Md}} - L_{\mathrm{Mq}})i_{\mathrm{Md}}i_{\mathrm{Mq}} \\ \psi_{\mathrm{Md}} = L_{\mathrm{Md}}i_{\mathrm{Md}} + \psi_0 \\ \psi_{\mathrm{Mq}} = L_{\mathrm{Mq}}i_{\mathrm{Mq}} \\ k_c = \frac{1.125lr_0\mu_0 k_{\mathrm{B0}}^2 N_{\mathrm{M}}^2}{\pi\delta_0^2} i_0^2 \\ k_{\mathrm{L}} = \frac{mP_{\mathrm{B}}P_{\mathrm{M}}}{4N_1 rP_{\mathrm{B}}} \\ k_{\mathrm{M}} = \frac{0.393P_{\mathrm{B}}P_{\mathrm{M}}L_{\mathrm{B}}}{N_1N_2lr\mu_0} \end{cases} \tag{1}$$

where ψ_{Md} and ψ_{Mq} represent the flux linkages produced by the torque winding; L_{Md} and L_{Mq} represent the self-inductance

component of the d-q shaft torque winding; i_{Md} and i_{Mq} are the current components of the shaft torque winding; M_{d} and M_{q} are the levitation force constants; i_{Bd} and i_{Bq} are the equivalent control currents for the d-q axis levitation force winding; ψ_0 represents the magnetic flux from the permanent magnet; i_0 denotes its equivalent magnetizing current.

According to the literature [18], the mathematical model of the levitation force of 3-DOF HMB can be expressed as:

$$\begin{cases} F_{\mathrm{x}} = \sqrt{3}k_{ir}i_{\mathrm{x}}/\sqrt{2} + 3k_{xy}x/2 \\ F_{\mathrm{y}} = \sqrt{3}k_{ir}i_{\mathrm{y}}/\sqrt{2} + 3k_{xy}y/2 \\ F_{\mathrm{z}} = k_{iz}i_{\mathrm{z}} + k_z z \end{cases} \tag{2}$$

where k_{ir} and k_{iz} represent the current coefficient; k_{xy} and k_z represent the displacement coefficient; i_x, i_y, and i_z represent the control current.

When establishing the motion equations for a 5-DOF-PMa-BSynRM, the rotor is treated as a rigid body, incorporating the effects of inter-axis coupling within the magnetic bearing system and its inherent gyroscopic behavior. The subscript "a" indicates the 3-DOF-HMB-related variables, and the subscript "b" indicates the 2-DOF-PMa-BSynRM-related variables.

The force analysis diagram for the rotor configuration is presented in Fig. 2, and the origin O coincides with the equilibrium position of the rotor's center of mass; T_{e} is the electromagnetic torque; l_a and l_b are the distances from the positions of the 3-DOF-HMB unit and the PMa-BSynRM unit to the equilibrium position of the rotor's center of mass; ω is the angular velocity of the rotor; T_{L} is the load torque; J_z is the moment of inertia of the rotor. The radial degrees of freedom correspond to the X and Y directions, respectively, while the axial degree of freedom corresponds to the Z direction. The corresponding forces are the radial suspension forces F_{ax}, F_{ay}, F_{bx}, F_{by}, and the axial suspension force F_{az}.

The system motion equation can be expressed as:

$$\begin{cases} m\ddot{x} = F_{ax} + F_{bx} \\ m\ddot{y} = F_{ay} + F_{by} \\ m\ddot{z} = F_{az} \\ J_x\ddot{\theta}_x = -l_a F_{ay} + l_b F_{by} - J_z\omega\dot{\theta}_y \\ J_y\ddot{\theta}_y = l_a F_{ax} - l_b F_{bx} + J_z\omega\dot{\theta}_x \\ \frac{J_z}{P_{\mathrm{M}}}\dot{\omega} = T_{\mathrm{e}} - T_{\mathrm{L}} \end{cases} \tag{3}$$

$$\begin{cases} \theta_x = \frac{y_a - y_b}{l_a + l_b} \\ \theta_y = \frac{x_a - x_b}{l_a + l_b} \\ x = \frac{l_b}{l_a + l_b}x_a + \frac{l_a}{l_a + l_b}x_b \\ y = \frac{l_b}{l_a + l_b}y_a + \frac{l_a}{l_a + l_b}y_b \\ z = z_a \end{cases} \tag{4}$$

where $J_x = J_y = J_d$ is the moment of inertia about the X and Y axes; F_{ax}, F_{ay}, F_{az}, F_{bx}, and F_{by} are the suspended forces on the five-directional rotors, respectively; x_a, y_a, z_a, x_b, and y_b are the corresponding rotor displacements in different directions.

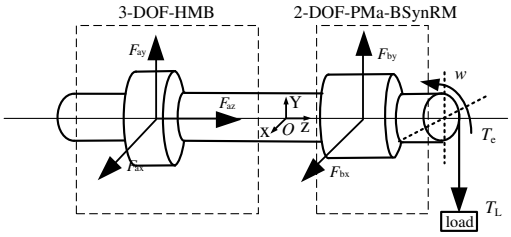

FIGURE 2. 5-DOF-PMa-BSynRM schematic diagram of rigid rotor structure.

2.3. Reversibility Analysis

The reversibility of the system is assessed using the Interactor algorithm. The 5DOFPMa-BSynRM contains 11 state variables:

$$\begin{aligned} \mathbf{X} &= (x_1, x_2, x_3, x_4, x_5, x_6, x_7, x_8, x_9, x_{10}, x_{11})^{\mathrm{T}} \\ &= (x_{\mathrm{a}}, y_{\mathrm{a}}, z_{\mathrm{a}}, x_{\mathrm{b}}, y_{\mathrm{b}}, \dot{x}_{\mathrm{a}}, \dot{y}_{\mathrm{a}}, \dot{z}_{\mathrm{a}}, \dot{x}_{\mathrm{b}}, \dot{y}_{\mathrm{b}}, \omega)^{\mathrm{T}} \end{aligned} \tag{5}$$

The input variables correspond to the control currents of the levitation force winding and torque winding. Input variables are formally expressed as:

$$\begin{aligned} \mathbf{U} &= (u_1, u_2, u_3, u_4, u_5, u_6, u_7)^{\mathrm{T}} \\ &= (i_{\mathrm{ax}}, i_{\mathrm{ay}}, i_{\mathrm{az}}, i_{\mathrm{Md}}, i_{\mathrm{Mq}}, i_{\mathrm{Bd}}, i_{\mathrm{Bq}})^{\mathrm{T}} \end{aligned} \tag{6}$$

The output variables are the five radial and axial displacements of the rotor along with its angular velocity. Output variables are formally expressed as:

$$\mathbf{Y} = (y_1, y_2, y_3, y_4, y_5, y_6)^{\mathrm{T}} = (x_{\mathrm{a}}, y_{\mathrm{a}}, z_{\mathrm{a}}, x_{\mathrm{b}}, y_{\mathrm{b}}, \omega)^T \tag{7}$$

Based on the definition of state variable X, the mapping relationship between state variables and output variables can be explicitly expressed through the system's output equation $Y = h(x)$, as follows:

$$Y = h(x) = \begin{cases} y_1 = x_1 \\ y_2 = x_2 \\ y_3 = x_3 \\ y_4 = x_4 \\ y_5 = x_5 \\ y_6 = x_{11} \end{cases} \tag{8}$$

Based on the dynamic motion Eq. (3) of the rotor, and substituting the expressions for electromagnetic force and torque (Eq. (1) and Eq. (2)), the state equation of the composite control object is derived, ultimately yielding the state equation of the composite control object as Eq. (9).

According to the Interactor algorithm and the aforementioned mapping relationship, computing the derivatives of the output Y until every component is explicitly incorporated in the input U. The first derivative of displacement output does not contain the input vector U. Therefore, the second derivative must be calculated to reveal components related to control current. For velocity output, the first derivative directly incorporates the current term responsible for torque generation. The result of this substitution is Eq. (10).

The expression for the Jacobi matrix is given by Eq. (11). Calculations show that rank $(\mathbf{A}) = 6$, and the relative order of the system is:

$$\boldsymbol{\alpha} = (\alpha_1, \alpha_2, \alpha_3, \alpha_4, \alpha_5, \alpha_6)^{\mathrm{T}} = (2, 2, 2, 2, 2, 1)^{\mathrm{T}} \tag{9}$$

The condition is satisfied: $\sum_{i=1}^{6}\alpha_i = 11$ (the number of state variables is 11). This indicates that the 5-DOF PMa-BSynRM system possesses system invertibility, and it can be represented by the following equations:

$$\begin{aligned}\mathbf{U} &= (u_1, u_2, u_3, u_4, u_5, u_6, u_7)^{\mathrm{T}} \\ &= \xi(\mathbf{X}, \ddot{y}_1, \ddot{y}_2, \ddot{y}_3, \ddot{y}_4, \ddot{y}_5, \dot{y}_6)\end{aligned} \tag{10}$$

$$\begin{cases}
\dot{x}_1 = x_6 \\
\dot{x}_2 = x_7 \\
\dot{x}_3 = x_8 \\
\dot{x}_4 = x_9 \\
\dot{x}_5 = x_{10} \\
\dot{x}_6 = \sqrt{\frac{3}{2}}k_{ir}\left(\frac{1}{m}+\frac{l_a^2}{J_d}\right)u_1 + k_d i_d\left(\frac{1}{m}-\frac{l_a l_b}{J_d}\right)u_2 \\
\quad +k_q\left(\frac{1}{m}-\frac{l_a l_b}{J_d}\right)u_4 u_6 + \frac{3}{2}k_{xy}\left(\frac{1}{m}+\frac{l_a^2}{J_d}\right)x_1 \\
\quad +\frac{J_z l_a x_{11}(x_9-x_8)}{J_d(l_a+l_b)} \\
\dot{x}_7 = \sqrt{\frac{3}{2}}k_{ir}\left(\frac{1}{m}-\frac{l_a l_b}{J_d}\right)u_1 + k_d i_d\left(\frac{1}{m}+\frac{l_b^2}{J_d}\right)u_2 \\
\quad +k_q\left(\frac{1}{m}+\frac{l_b^2}{J_d}\right)u_4 u_6 + \frac{3}{2}k_{xy}\left(\frac{1}{m}-\frac{l_a l_b}{J_d}\right)x_1 \\
\quad +\frac{J_z l_b x_{11}(x_9-x_8)}{J_d(l_a+l_b)} \\
\dot{x}_8 = \sqrt{\frac{3}{2}}k_w\left(\frac{1}{m}+\frac{l_a^2}{J_d}\right)u_3 - k_d i_d\left(\frac{1}{m}-\frac{l_a l_b}{J_d}\right)u_4 \\
\quad +k_q\left(\frac{1}{m}-\frac{l_a l_b}{J_d}\right)u_2 u_6 + \frac{3}{2}k_{xy}\left(\frac{1}{m}+\frac{l_a^2}{J_d}\right)x_3 \\
\quad +\frac{J_z l_a x_{11}(x_9-x_8)}{J_d(l_a+l_b)} \\
\dot{x}_9 = \sqrt{\frac{3}{2}}k_{ir}\left(\frac{1}{m}-\frac{l_a l_b}{J_d}\right)u_3 - k_d i_d\left(\frac{1}{m}+\frac{l_b^2}{J_d}\right)u_4 \\
\quad +k_q\left(\frac{1}{m}+\frac{l_b^2}{J_d}\right)u_2 u_6 + \frac{3}{2}k_{xy}\left(\frac{1}{m}-\frac{l_d l_b}{J_d}\right)x_3 \\
\quad +\frac{J_z l_b x_{11}(x_9-x_8)}{J_d(l_a+l_b)} \\
\dot{x}_{10} = \frac{k_z x_5 + k_{iz}u_5 \dot{x}_{11}}{m} \\
\dot{x}_{11} = \frac{\frac{3}{2}P_{\mathrm{M}}^2(L_d-L_q)i_d u_6 - P_{\mathrm{M}}T_L}{J_z}
\end{cases} \tag{11}$$

$$\begin{cases}
\dot{y}_1 = x_6 \\
\ddot{y}_1 = \sqrt{\frac{3}{2}}k_{ir}\left(\frac{1}{m}+\frac{l_a^2}{J_d}\right)u_1 + k_d i_d\left(\frac{1}{m}-\frac{l_a l_b}{J_d}\right)u_2 \\
\quad +k_q\left(\frac{1}{m}-\frac{l_a l_b}{J_d}\right)u_4 u_6 + \frac{3}{2}k_{xy}\left(\frac{1}{m}+\frac{l_a^2}{J_d}\right)x_1 \\
\quad +\frac{J_z l_a}{J_d(l_a+l_b)}x_{11}(x_9-x_8) \\
\dot{y}_2 = x_7 \\
\ddot{y}_2 = \sqrt{\frac{3}{2}}k_{ir}\left(\frac{1}{m}-\frac{l_a l_b}{J_d}\right)u_1 + k_d i_d\left(\frac{1}{m}+\frac{l_b^2}{J_d}\right)u_2 \\
\quad +k_q\left(\frac{1}{m}+\frac{l_b^2}{J_d}\right)u_4 u_6 + \frac{3}{2}k_{xy}\left(\frac{1}{m}-\frac{l_a l_b}{J_d}\right)x_1 \\
\quad +\frac{J_z l_b}{J_d(l_a+l_b)}x_{11}(x_9-x_8) \\
\dot{y}_3 = x_8 \\
\ddot{y}_3 = \sqrt{\frac{3}{2}}k_{ir}\left(\frac{1}{m}+\frac{l_a^2}{J_d}\right)u_3 - k_d i_d\left(\frac{1}{m}-\frac{l_a l_b}{J_d}\right)u_4 \\
\quad +k_q\left(\frac{1}{m}-\frac{l_a l_b}{J_d}\right)u_2 u_6 + \frac{3}{2}k_{xy}\left(\frac{1}{m}+\frac{l_a^2}{J_d}\right)x_3 \\
\quad +\frac{J_z l_a}{J_d(l_a+l_b)}x_{11}(x_9-x_8) \\
\dot{y}_4 = x_9 \\
\ddot{y}_4 = \sqrt{\frac{3}{2}}k_{br}\left(\frac{1}{m}-\frac{l_a l_b}{J_d}\right)u_3 - k_d i_d\left(\frac{1}{m}+\frac{l_b^2}{J_d}\right)u_4 \\
\quad +k_q\left(\frac{1}{m}+\frac{l_b^2}{J_d}\right)u_2 u_6 + \frac{3}{2}k_{xy}\left(\frac{1}{m}-\frac{l_a l_b}{J_d}\right)x_3 \\
\quad +\frac{J_z l_b}{J_d(l_a+l_b)}x_{11}(x_9-x_8) \\
\dot{y}_5 = x_{10} \\
\ddot{y}_5 = \frac{1}{m}k_z x_5 + \frac{1}{m}k_{iz}u_5 \\
\dot{y}_6 = \frac{3P_{\mathrm{M}}^2}{2J_z}\left[\psi_0\, u_6 + (L_d - L_q)i_d u_6\right] - \frac{P_{\mathrm{M}}}{J_z}T_L
\end{cases} \tag{12}$$

$$\mathbf{A} = \left[\frac{\partial(\ddot{y}_1, \ddot{y}_2, \ddot{y}_3, \ddot{y}_4, \ddot{y}_5, \dot{y}_6)}{\partial \mathbf{U}}\right]$$

$$= \begin{bmatrix}
\sqrt{\frac{3}{2}}k_{ir}\left(\frac{1}{m}+\frac{l_a^2}{J_d}\right) & k_d i_d\left(\frac{1}{m}-\frac{l_a l_b}{J_d}\right) & 0 \\
\sqrt{\frac{3}{2}}k_{ir}\left(\frac{1}{m}-\frac{l_a l_b}{J_d}\right) & k_d i_d\left(\frac{1}{m}+\frac{l_a^2}{J_d}\right) & 0 \\
0 & k_q\left(\frac{1}{m}-\frac{l_a l_b}{J_d}\right)u_6 & \sqrt{\frac{3}{2}}k_{ir}\left(\frac{1}{m}+\frac{l_a^2}{J_d}\right) \\
0 & k_q\left(\frac{1}{m}+\frac{l_a^2}{J_d}\right)u_6 & \sqrt{\frac{3}{2}}k_{ir}\left(\frac{1}{m}-\frac{l_a l_b}{J_d}\right) \\
0 & 0 & 0 \\
0 & 0 & 0
\end{bmatrix}$$

$$\begin{bmatrix}
k_q\left(\frac{1}{m}-\frac{l_a l_b}{J_d}\right)u_6 & 0 & k_q\left(\frac{1}{m}-\frac{l_a l_b}{J_d}\right)u_4 \\
k_q\left(\frac{1}{m}+\frac{l_a^2}{J_d}\right)u_6 & 0 & k_q\left(\frac{1}{m}+\frac{l_a^2}{J_d}\right)u_4 \\
-k_d i_d\left(\frac{1}{m}-\frac{l_a l_b}{J_d}\right) & 0 & k_q\left(\frac{1}{m}-\frac{l_a l_b}{J_d}\right)u_2 \\
-k_d i_d\left(\frac{1}{m}+\frac{l_a^2}{J_d}\right) & 0 & k_q\left(\frac{1}{m}+\frac{l_a^2}{J_d}\right)u_2 \\
0 & \frac{1}{m}k_{iz} & 0 \\
0 & 0 & \frac{3P_{\mathrm{M}}^2}{2J_z}[\psi_0 + (L_d - L_q)i_d]
\end{bmatrix} \tag{13}$$

3. ESTABLISHMENT OF THE MAMDANI-FNN INVERSE SYSTEM

3.1. FNN Structure and Working Principle

The structure of the fuzzy neural network based on Mamdani reasoning is shown in Fig. 3. The algorithm and data processing process of each layer are as follows:

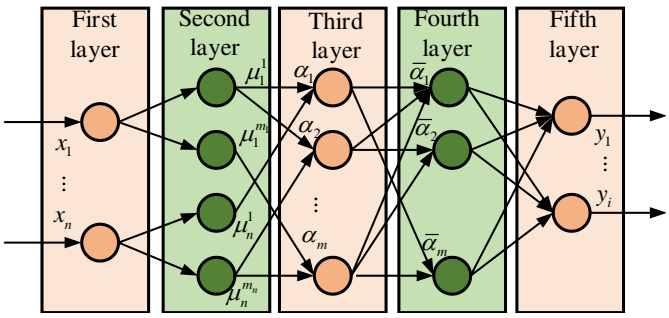

FIGURE 3. Structure of the FNN.

Layer 1-input layer: The input value $x = (x_1, x_2, \ldots, x_n)$ is sent to the next layer. Number of nodes in this layer: $N_1 = n$.

Layer 2-blurring layer: Calculate the membership function μ_i^j of each input component belonging to the fuzzy set of language variable values, and calculate the membership degree of the input value belonging to each fuzzy set through the membership function.

$$\mu_i^j = \mu_{A_i^j}(x_i) \tag{14}$$

where $i = 1, 2, \ldots, n$, $j = 1, 2, \ldots, m_i$; n is the number of input quantities; m_i represents the fuzzy segmentation number of x_i.

This study utilizes a Gaussian-shaped membership function, which can be expressed as:

$$\mu_{A_i^k}(x_i) = \exp\left[-\left(\frac{x_i - \alpha_i^k}{\sigma_i^k}\right)^2\right] \tag{15}$$

where α_i^k and σ_i^k are the center and width of the membership function, respectively, and the total number of nodes in this layer can be expressed as:

$$N_2 = \sum_{i=1}^{n} m_i \tag{16}$$

Layer 3-rules layer: This layer combines the fuzzified inputs according to the antecedents of the fuzzy rules. Each node corresponds to one fuzzy rule and performs antecedent matching. The computation can be expressed as follows:

$$\alpha_j = \min\{\mu_1^{i_1}, \mu_2^{i_2}, \ldots, \mu_n^{i_n}\} \tag{17}$$

where $i_1 = \{1, 2, \ldots, m_1\}$, $i = 2\{1, 2, \ldots, m_2\}, \ldots,$ $i_n = \{1, 2, \ldots, m_n\}$, $j_n = \{1, 2, \ldots, m\}$, $m = \prod_{i=1}^{n} m_i$. The node count of this layer: $N_3 = m$.

Layer 4-reasoning layer: the system performs normalization calculations to obtain fuzzy inference results. Let the number of nodes in this layer equal that of the third layer: $N_4 = N_3 = m$, and the calculation formula can be expressed as:

$$\bar{\alpha}_j = \frac{\alpha_j}{\sum_{j=1}^{m} \alpha_j}, \quad j = 1, 2, \ldots, m \tag{18}$$

Layer 5-output layer: The result obtained from fuzzy reasoning undergoes defuzzification calculation, with the formula expressed as:

$$y_i = \sum_{j=1}^{m} w_{ij} \bar{\alpha}_j, \quad i = 1, 2, \ldots, r \tag{19}$$

where w_{ij} is equivalent to the central value of the j language value belonging function.

3.2. Construction of the Inverse System

The method proposed in this paper utilizes an improved genetic algorithm (IGA) to adjust the number of FNN rules as well as the centers and widths of the membership functions, thereby accelerating the decoupling process.

Traditional genetic algorithms (GAs) map the chromosome evolution process through computers, including biological evolution phenomena, such as selection, crossover, and mutation, ultimately seeking the optimal solution. The execution of the algorithm primarily involves: encoding the practical problem, generating an initial chromosome population, computing fitness values, and performing genetic operations. Genetic operations mainly include selection, crossover, and mutation. Selection mechanisms commonly employ the roulette wheel method, tournament selection, and elitist preservation. In conventional genetic algorithms, the roulette wheel model assigns a selection probability to each individual that is proportional to its fitness value. This probability can be formulated as follows:

$$p_i = \frac{F(z_i)}{\sum_{j=1}^{n} F(z_j)} \tag{20}$$

where $F(z)$ is the fitness function of an individual, and z is a vector composed of various elements as the optimization target.

The roulette wheel model selection process is not applicable to small-scale populations. Therefore, the improved genetic algorithm employed in this paper combines the roulette wheel selection method with an elite retention strategy: calculate the fitness value f_i for all individuals in the current population based on the fitness curve, sort them from the highest to the lowest, and select the top N_{elite} individuals as elites to be directly copied into the next generation. The remaining individuals are generated through the application of genetic operators. The IGA ensures that rare samples have a chance to be retained, maintaining population diversity and avoiding premature convergence. A schematic of the GA workflow is provided in Fig. 4.

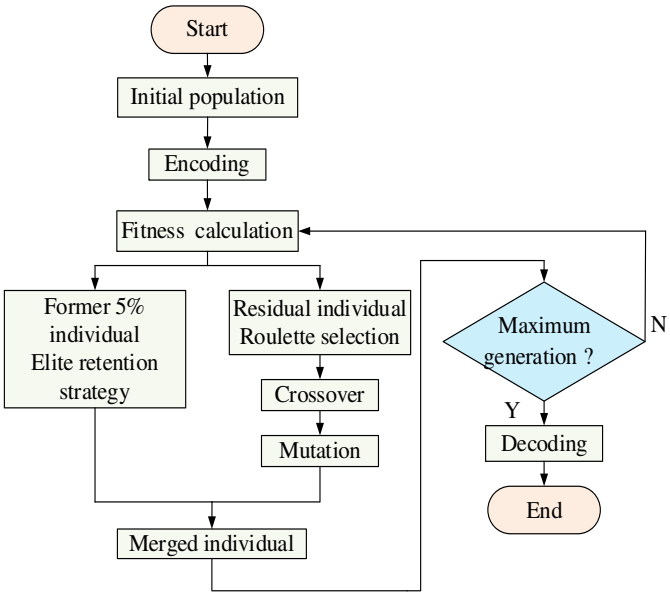

FIGURE 4. Flowchart of genetic algorithm.

To effectively optimize the parameters of the fuzzy neural network, this paper adopts real-number encoding. Based on the optimization objective, the chromosome vector Z is constructed by concatenating the rule number, the center of the Gaussian membership function, and the width. The chromosome can be defined as:

$$Z = [N_r, c_{11}, c_{12}, \ldots, c_{nm}, \sigma_{11}, \sigma_{12}, \ldots, \sigma_{nm}] \tag{21}$$

where n denotes the number of input nodes, and m represents the number of fuzzy partitions.

The root mean square error (RMSE) between FNN output and target training data was adopted as the primary performance metric. Since the objective of IGA is to minimize this error,

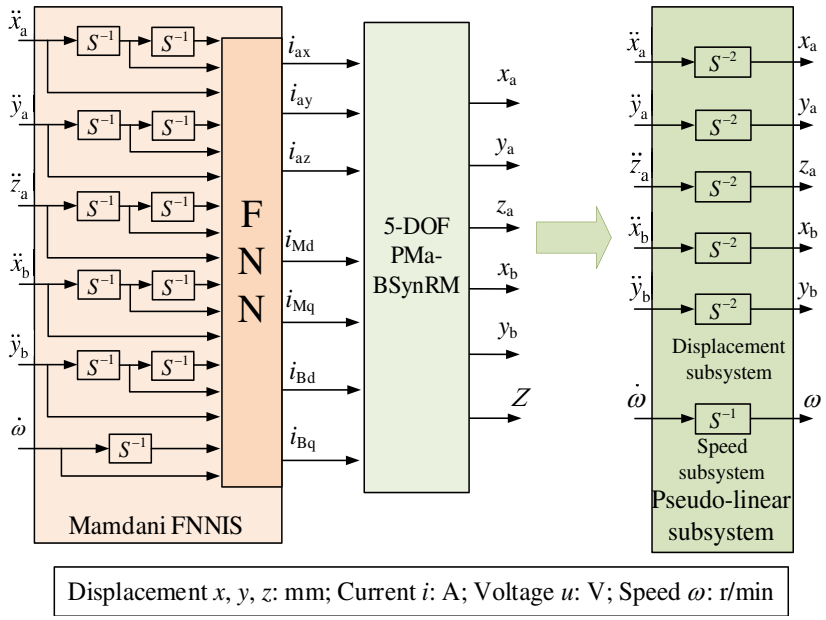

FIGURE 5. Pseudo-linear subsystems.

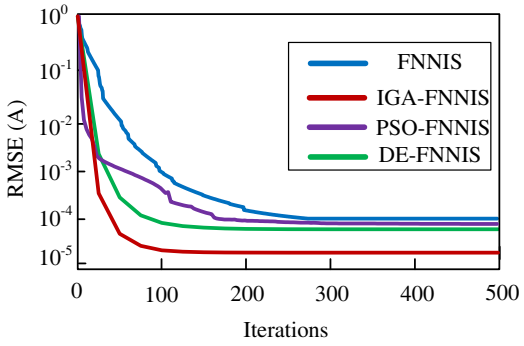

FIGURE 6. Training error curve.

the fitness function $F(Z)$ was designed to be inversely proportional to the network's RMSE:

$$F(Z) = \frac{1}{RMSE + \varepsilon} = \frac{1}{\sqrt{\frac{1}{K}\sum_{k=1}^{K}(y_d(k) - y(k))^2 + \varepsilon}} \quad (22)$$

where K denotes the total number of training samples; $y_d(k)$ is the expected output; $y(k)$ is the actual output of the FNN; and ε is the standard deviation.

In this paper, the FNN is employed to construct the inverse system of the PMa-BSynRM. The parameters of the FNN are trained using the IGA. Offline training is adopted to adjust the neural network parameters until the error meets the accuracy requirements.

Firstly, the initial phase involves the implementation of a closed-loop system for the 5-DOF-PMa-BSynRM to generate the dataset required for training the neural network. Random displacement signals and angular velocity signals within the operating range are used as excitations, with a sampling time of 0.5 ms and an operation time of 5 s. Ten thousand datasets are obtained, of which 80% are used for training and the remaining 20% for testing. The sampled signals include displacement signals x_a, y_a, z_a, x_b, y_b, current signals i_{ax}, i_{ay}, i_{az}, i_{Md}, i_{Mq}, i_{Bd}, i_{Bq}, and rotational speed signal ω.

Secondly, optimize the number of rules (N_r), membership function centers and widths in fuzzy neural networks using the IGA. The population size is set to 100 with a maximum iteration count of $G_{\max} = 500$. The elite retention strategy preserves the top five individuals. The crossover rate is set to 0.60, and the mutation rate is set to 0.01. A crossover rate of 0.60 ensures sufficient genetic diversity for comprehensive global search, while a low mutation rate of 0.01 prevents the algorithm from trapping in local optima without disrupting the convergence stability of the FNN parameters. The optimized FNN parameters after final refinement: the number of input layer nodes $N_1 = 17$; the number of fuzzy layer nodes $N_2 = 51$; the number of fuzzy segments $m_i = 3$; the number of rule layer nodes $N_3 = 42$; the number of inference layer nodes $N_4 = N_3 = 42$; the number of output layer nodes $N_5 = 7$; the learning rate $\eta = 0.01$; and the training iteration count is 500. The input and output membership functions are selected as Gaussian and trigonometric functions, respectively, while the defuzzification method employs the centroid approach. After training, the optimal FNN model is output.

Finally, the optimized fuzzy neural network is integrated with 11 integrators to form a fuzzy neural network inverse system (FNNIS) for the PMa-BSynRM. This system is then connected in series with the original nonlinear plant, thereby decoupling it into five second-order displacement pseudo-linear subsystems and one first-order angular velocity pseudo-linear subsystem, as illustrated in Fig. 5.

As illustrated in Fig. 5, the proposed method transforms the original strongly coupled multivariable system into independent single-input single-output pseudo-linear subsystems through precise approximation of nonlinear mappings. Expanding from subsystem-level analysis to the global 5-DOF

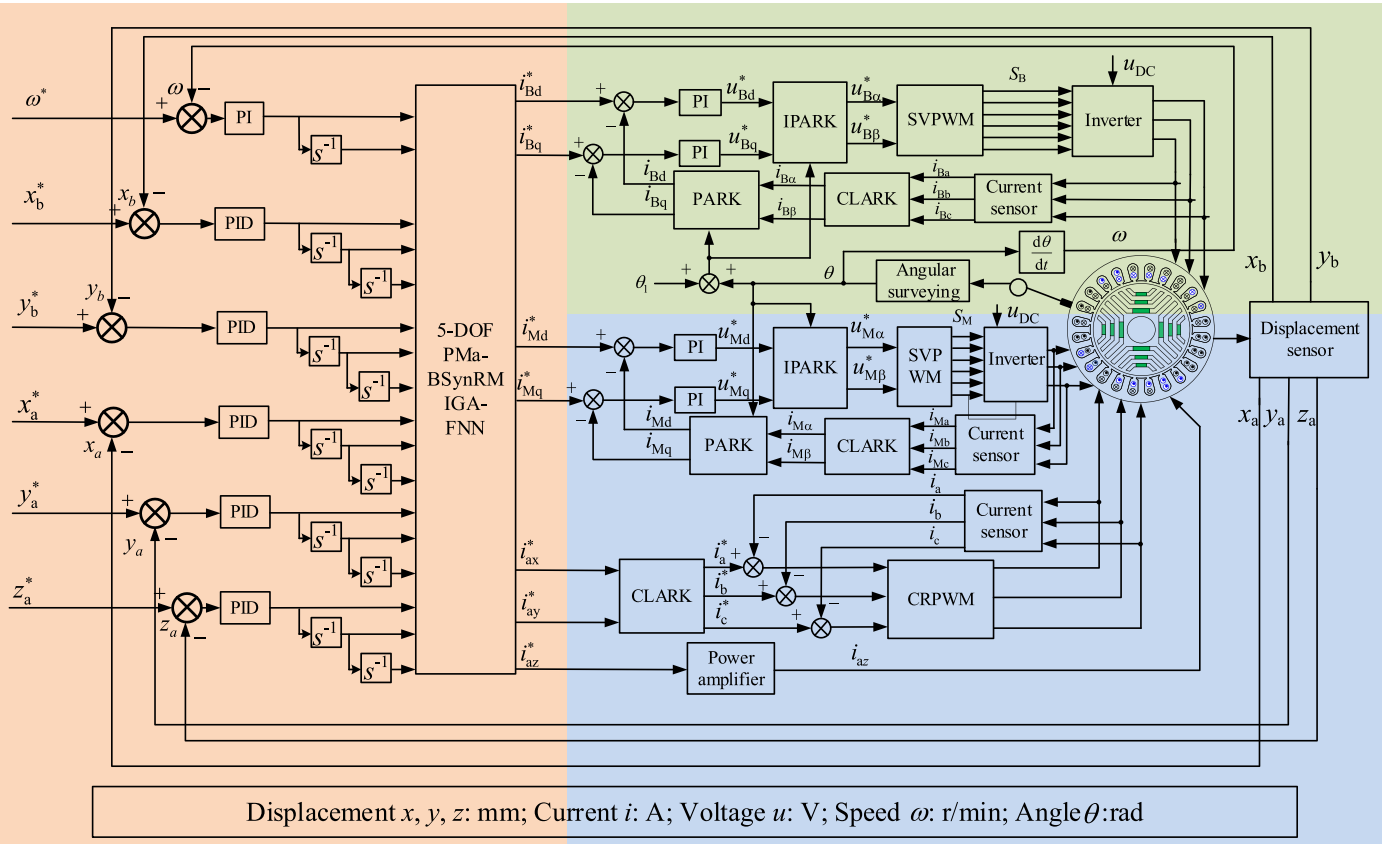

FIGURE 7. PMa-BSynRM dynamic decoupling control system.

system only increases the number of independent pseudo-linear subsystems without fundamentally altering the core logic of decoupled control. From an electromagnetic physics perspective, the coupling characteristics of the 5-DOF system are strictly confined to two physically isolated regions: the torque-suspension force coupling within the 2-DOF-PMa-BSynRM assembly and the radial-axial coupling within the 3-DOF-HMB component. The primary coupling mechanism between magnetic bearings and motors is mechanical coupling. Therefore, given that the 5-DOF prototype is currently undergoing optimization and debugging, the proposed method's feasibility can be validated through 2-DOF and 3-DOF subsystem experiments in subsequent experimental phases.

To validate the superior fitting performance of the IGA-FNNIS method, comparative experiments using FNNIS, PSO-FNNIS, and DE-FNNIS methods were conducted. The root mean square error (RMSE) between expected values and measured values was employed as the evaluation metric to compare the fitting performance of the decoupled models constructed by the four methods.

Figure 6 shows the error comparison curve. As shown in Fig. 6, the IGA-FNNIS model converges at 122 iterations with an RMSE of 3.22E-5. In contrast, the DE-FNNIS method converged after 175 iterations with an RMSE of 8.26E-5; the PSO-FNNIS method converged after 215 iterations with an RMSE of 1.04E-4, while the FNNIS model converged after 274 iterations with an RMSE of 1.68E-4. The IGA-FNNIS model achieved 30.3% fewer iterations and 61% lower error than the DE-FNNIS model; 43.3% fewer iterations and 69% lower error than PSO-FNNIS; and 55.5% fewer iterations and 80.8% lower error than the FNNIS model. These results demonstrate that the improved fuzzy neural network inverse system significantly accelerates decoupling processes and enhances control accuracy. The overall control block diagram is shown in Fig. 7.

4. SIMULATION TEST

4.1. Dynamic Decoupling Simulation

To confirm the effectiveness of the proposed control method, 5-DOF-PMa-BSynRM is taken as the research object. The proposed method is simulated in MATLAB/Simulink environment, and the magnetic field orientation control method (FOC) and FNNIS control method are selected for comparative analysis.

Considering the effect of gravity, in the simulation, the initial position of the rotor is set as $x = x_a = x_b = 0$ mm, $y = y_a = y_b = -0.2$ mm, $z = z_a = -0.2$ mm; the equilibrium position is $x = x_a = x_b = 0$ mm, $y = y_a = y_b = 0$ mm, $z = z_a = 0$ mm; the given speed of the motor is 5000 r/min.

The dynamic decoupling performance comparison simulation curve of PMa-BSynRM is shown in Fig. 8. After the motor speed stabilizes at 3000 r/min, at $t = 0.25$ s, the given speed is changed from 3000 r/min to 5000 r/min suddenly. In Fig. 8, the FOC has a settling time of 52 ms to reach a steady speed of 5000 r/min, featuring a peak speed deviation of 86 r/min, and the peak fluctuations in radial displacements are 22 μm and

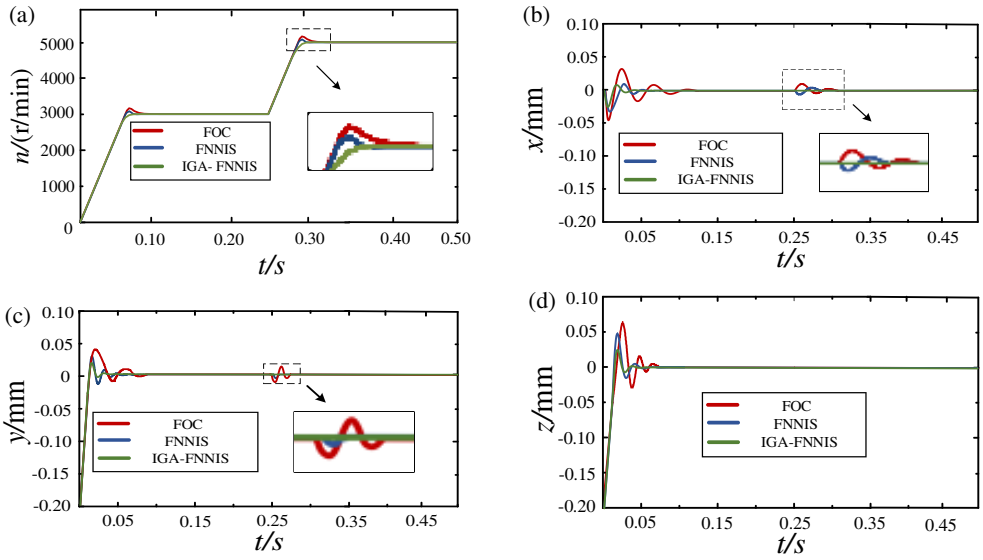

FIGURE 8. Speed and displacement curves: (a) Speed; (b) x; (c) y; (d) z.

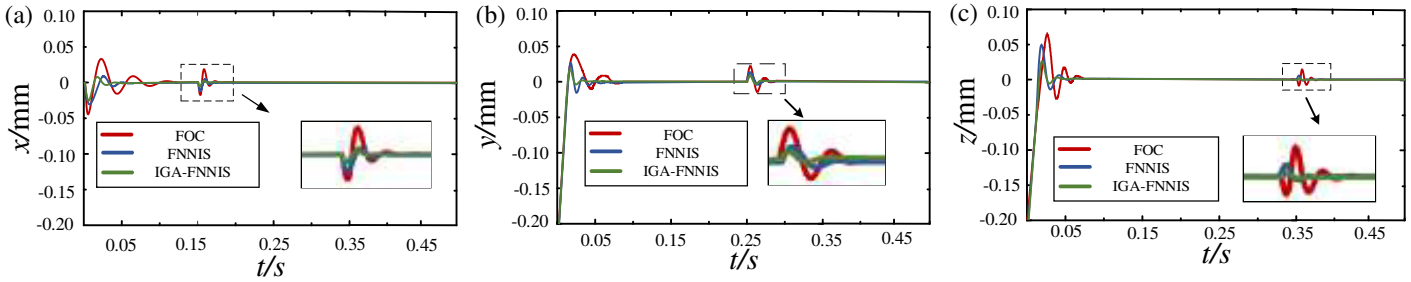

FIGURE 9. Anti-interference performance of the PMa-BSynRM: (a) x; (b) y; (c) z.

25 µm. The FNNIS has a settling time of 38 ms to reach a steady speed of 5000 r/min, featuring a peak speed deviation of 32 r/min, and the peak fluctuations in radial displacements are 14 µm and 16 µm. The proposed method stabilizes the speed at 32 ms, representing a reduction of 38.5% and 15.8% compared to the FOC and FNNIS methods, respectively, while virtually no offset in the x-, y-, and z-directions. The results demonstrate that the proposed control method better achieves stable decoupling between electromagnetic torque and levitation force.

4.2. Anti-Interference Simulation

Figure 9 presents a comparison of the anti-interference performance of the PMa-BSynRM through simulation results. Upon stable suspension of the rotor, interference forces of 20 N are exerted on the rotor along the x-, y-, and z-directions at 0.15 s, 0.25 s, and 0.35 s, respectively. As shown in Fig. 9, for the FOC method, the rotor's displacement magnitudes due to interference forces in the x-, y-, and z-directions are approximately 42 µm, 45 µm, and 44 µm, respectively. Under the FNNIS control method, the fluctuations are 28 µm, 30 µm, and 25 µm, respectively. In contrast, the proposed method produced fluctuations of only 16 µm, 19 µm, and 14 µm, representing reductions of 61.9%, 57.8%, and 68.2% in displacement peaks compared to the FOC method, and 42.9%, 36.7%, and 44.0%, respectively, compared to the FNNIS method. The test results indicate that under the IGA-FNNIS, the anti-interference capability of PMa-BSynRM is effectively enhanced.

4.3. Decoupled Simulation of the Suspension Forces

The 5-DOF PMa-BSynRM was stably suspended at the equilibrium position at a rotational speed of 5000 r/min. At $t = 0.05$ s, 0.125 s, 0.20 s, 0.275 s, and 0.35 s, pulse signals with a duration of 0.05 s and an amplitude of 50 µm were sequentially applied to the rotor's displacement in five degrees of freedom. Fig. 10 shows the decoupling performance curves among the various levitation forces of the 5-DOF-PMa-BSynRM.

As shown in Fig. 10(a), for the FOC control method, the time required for displacement x_a to rise to 50 µm is 15 ms, with a displacement response overshoot of approximately 17 µm. For the FNNIS control method, the rise time for displacement x_a to reach 50 µm is 12 ms, with a displacement overshoot of approximately 8 µm. The proposed control method achieves only a 9 ms rise time with negligible displacement overshoot. Compared to the traditional FOC method, the system's rise time is reduced by 40%; compared to the FNNIS method, the rise time is also shortened by 25%. Simultaneously, as evident from Figs. 10(b), (c), (d), and (e), under the IGA-FNNIS control method, individual displacement changes remain unaffected by others, effectively achieving decoupling among degrees of freedom.

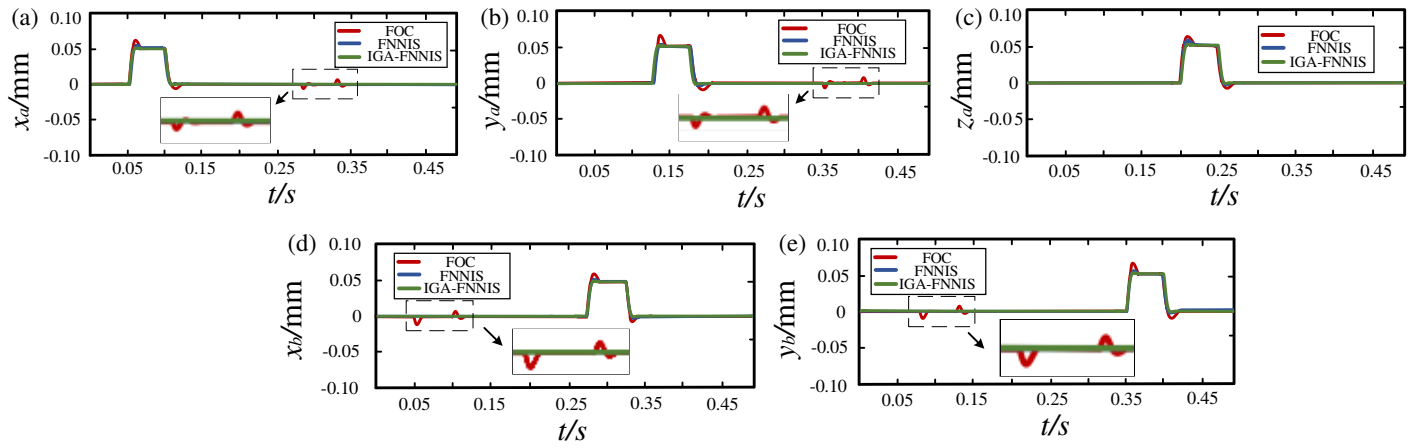

FIGURE 10. Comparative performance of decoupling control on suspension force displacement simulation: (a) x_a; (b) y_a; (c) z_a; (d) x_b; (e) y_b.

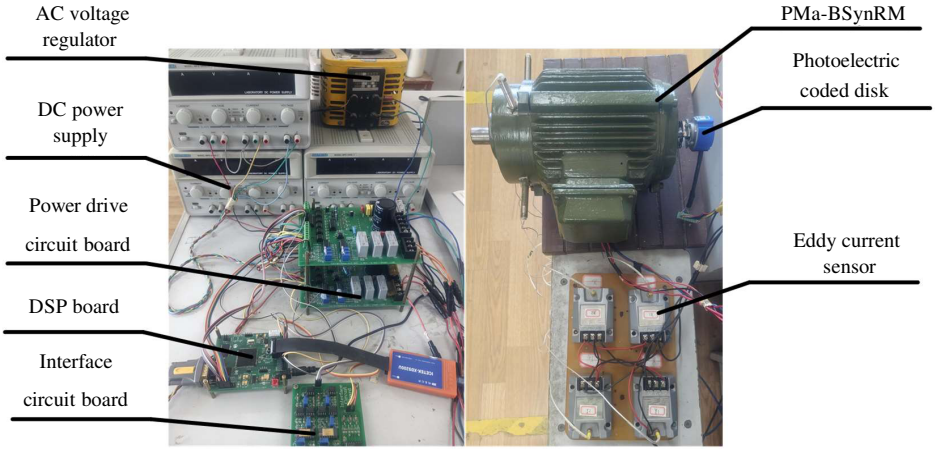

FIGURE 11. The experimental platform of PMa-BSynRM.

5. EXPERIMENTAL VALIDATION ON SUBSYSTEMS

The 5-DOF-PMa-BSynRM experimental test bed is currently under development, so experimental validation is conducted using subsystems with 2-DOF-PMa-BSynRM and HMB. Experimental validation was conducted for both subsystems to confirm the effectiveness of the proposed algorithm in addressing strongly coupled magnetic field problems. Comparative experiments were conducted simultaneously using the FNNIS and FOC methods.

The system controller utilizes a TMS320F28335 controller with an interrupt frequency set at 10 kHz. To evaluate practical deployment, the IGA-FNNIS computational load was profiled on the TMS320F28335 digital signal processor (DSP). The system's control cycle is strictly limited to within 100 µs, utilizing static memory allocation. Performance analysis indicates that the execution time of IGA FNNIS is approximately 32.8 µs per cycle, fully complying with the 100 µs hardware constraint and 0.5 ms data sampling period requirements. Furthermore, its static memory footprint is 36.4 KB of ROM and 16.5 KB of RAM, safely within the DSP's capacities (512 KB ROM, 68 KB RAM). This confirms the method's real-time feasibility without control delays or memory overflow.

The system collects radial displacement signals via eddy current sensors, which are converted into voltage signals through a displacement interface circuit. After DSP processing, pulse width modulation signals are generated and amplified by the power driver board to produce three-phase control currents. The basic parameters of PMa-BSynRM used in the experiment are shown in Table 2. The complete experimental platform structure is illustrated in Fig. 11.

5.1. Dynamic Decoupling Experiment of System

To dynamically decouple performance and enhance dynamic robustness, a variable-speed experiment was conducted as shown in Fig. 12. After the motor stabilized at 3000 r/min, the target speed was abruptly increased to 5000 r/min, creating a significant dynamic disturbance scenario through this abrupt acceleration process.

At this point, the FOC method's speed stabilizes after 112 ms with an overshoot of 4.6%. Due to the change in speed, the rotor exhibits the magnitudes of 48 µm and 51 µm in the x- and y-directions. The FNNIS method speed stabilizes after 98 ms with an overshoot of 2.3%, and the magnitudes of the rotor's disturbance are 32 µm and 35 µm in the x- and y-directions. The IGA-FNN method has almost no overshoot, with a regu-

TABLE 2. Parameters and description of the experimental platform.

Parameters	Value	Parameters	Value
Rated voltage U (V)	220	Air gap δ_0 (mm)	0.25
Rated power P (kW)	1.1	Volume (mm^3)	$4 \times (120 \times 71 \times 73)$
n (r/min)	500	m_r (kg)	1.6
Ψ_0 (Wb)	0.0359	Rotational inertia J (kg $\cdot$ mm^2)	5.6×10^{-4}
P_M/P_B	2/1	L_B (mH)	2.34

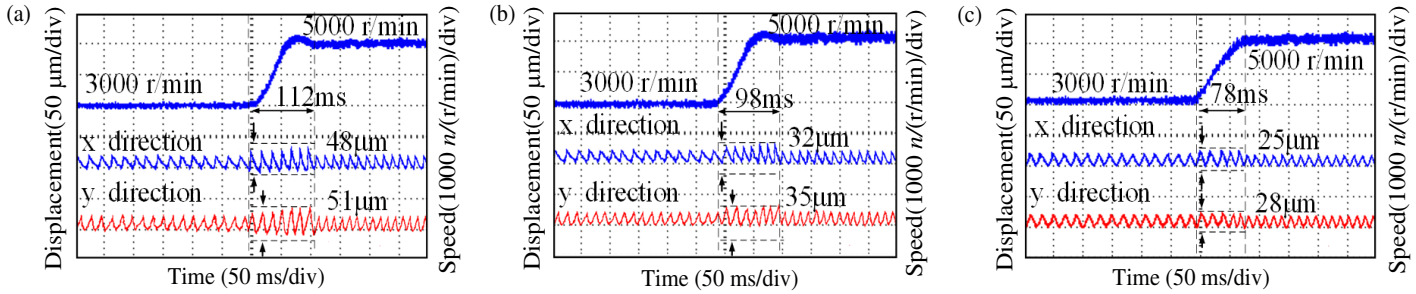

FIGURE 12. Speed and radial displacement in the x- and y-direction: (a) FOC; (b) FNNIS; (c) IGA-FNNIS.

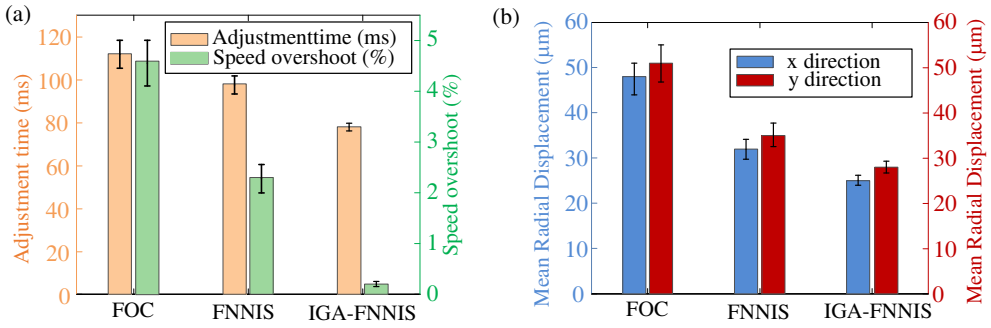

FIGURE 13. Statistical analysis results: (a) Adjustment time and speed overshoot; (b) Mean radial displacement in the x- and y-directions.

lation time of 78 ms, and the radial vibration amplitudes of the rotor are reduced to 25 μm and 28 μm in the x- and y-directions. Compared to the FOC method and FNNIS method, the adjustment time was reduced by 30.4% and 20.4%, respectively; the x-direction displacement fluctuation was decreased by 47.9% and 45.1%, respectively; and the y-direction displacement fluctuation was reduced by 45.1% and 20.0%, respectively. Fig. 13 primarily presents the statistical analysis results of the system during dynamic decoupling experiments. The error bars labeled above the bar charts visually demonstrate the dispersion level and extreme value range of displacement fluctuations throughout this dynamic process. Comparative experimental results show that the proposed control methods can enhance the system's resistance to interference and better achieve decoupling control between suspension forces.

5.2. Anti-Interference Experiment

The anti-interference experimental results of PMa-BSynRM are shown in Fig. 14. When the motor is operating stably, a force of 10 N is applied at a point along the y-axis direction of the rotor. When the FOC method is employed, the radial deflection of the rotor in the y direction is 48 μm, and that in the x direction is 43 μm, with an adjustment time of 142 ms. For the FNNIS method, the rotor displacement fluctuation was 40 μm in the y-axis direction and 37 μm in the x-axis direction, with an adjustment time of 109 ms.

When employing the IGA-FNNIS method, under disturbance forces, the rotor deviates from the equilibrium point by up to 30 μm in the y direction while exhibiting only 25 μm displacement along the x direction, with the adjustment time reduced to 76 ms. Compared to the FOC method and FNNIS method, the y direction single fluctuation decreases by 37.5% and 25.0%, respectively; the x direction single fluctuation decreases by 41.9% and 32.4%, respectively; and the adjustment time is shortened by 46.5% and 30.3%, respectively. Fig. 15 presents the statistical comparison results of the system's anti-interference performance test, including adjustment time and radial displacement fluctuations. Experimental results demonstrate that the proposed control method significantly enhances the system's anti-interference capability while achieving more precise decoupling control of suspension forces.

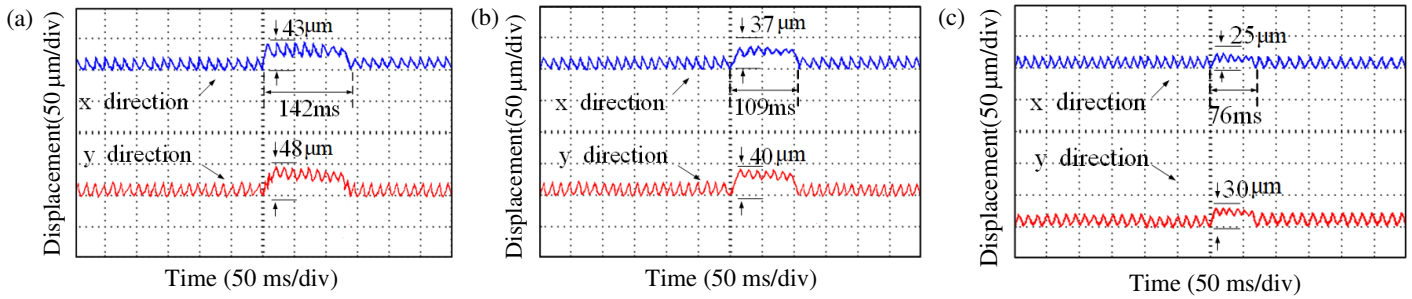

FIGURE 14. Radial displacement: (a) FOC; (b) FNNIS; (c) IGA-FNNIS.

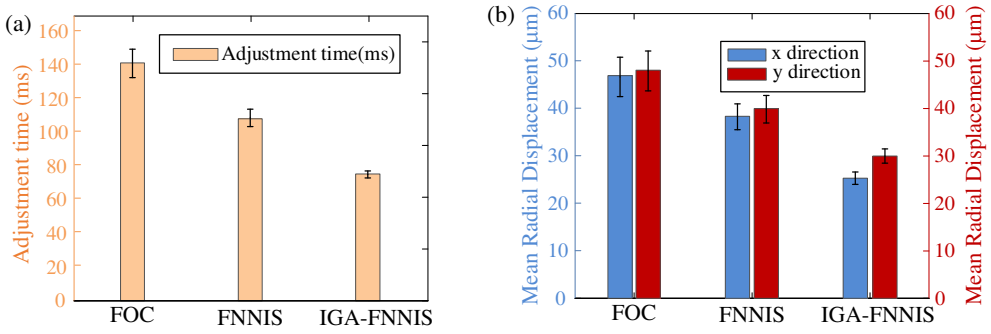

FIGURE 15. Statistical comparison of anti-interference performance: (a) Adjustment time; (b) Mean radial displacement in the x- and y-directions.

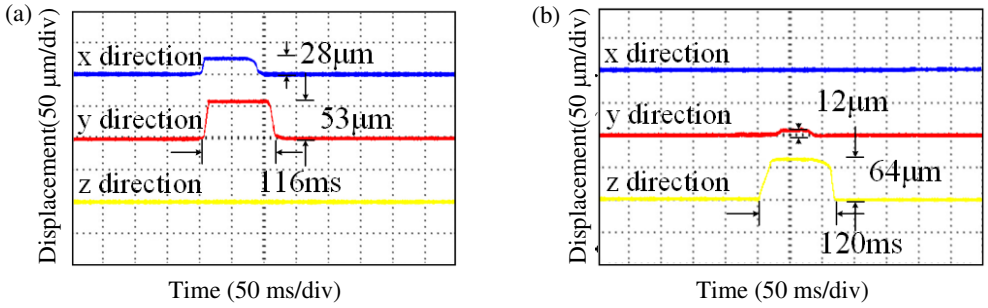

FIGURE 16. FOC control method: (a) Radial anti-interference curve; (b) Axial anti-interference curve.

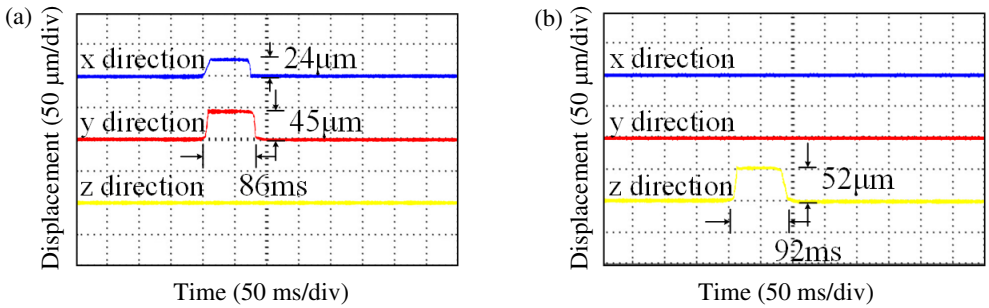

FIGURE 17. FNNIS control method: (a) Radial anti-interference curve; (b) Axial anti-interference curve.

The anti-interference test results of HMB are shown in Figs. 16–18. After achieving stable suspension of HMB, external disturbance forces of 2 N were applied in both radial and axial directions. In the radial experiment, the FOC method caused rotor displacement fluctuations of 53 μm in the y direction and 28 μm in the x direction, with a recovery time of 116 ms. When the FNNIS method is used, displacement disturbances reached 45 μm in the y direction and 24 μm in the x direction, with a recovery time of 86 ms. In contrast, the IGA-FNNIS control method reduced y direction displacement fluctuations to 30 μm, representing decreases of 43.4% and 33.3% compared to FOC and FNNIS methods, respectively. For the x direction, displacement fluctuations decreased to 12 μm, showing reductions of 57.1% and 50.0% compared to FOC and FNNIS methods. The stable recovery time was shortened to 64 ms, with recovery time reductions of 44.8% and 25.6%, respectively.

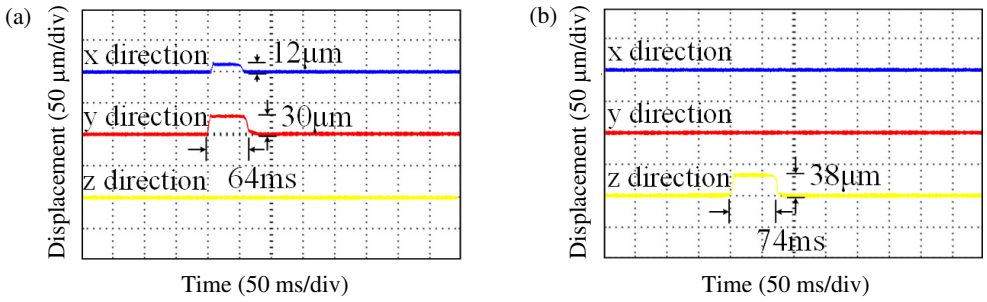

FIGURE 18. IGA-FNNIS control method: (a) Radial anti-interference curve; (b) Axial anti-interference curve.

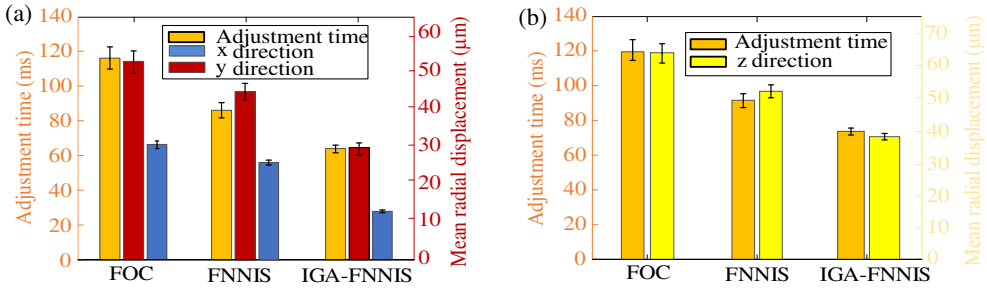

FIGURE 19. Statistical comparison of anti-interference performance of 3-DOF-HMB: (a) Adjusting time and radial displacement; (b) Adjusting time and axial displacement.

In the axial anti-interference experiment, the FOC and FNNIS control methods exhibited z direction displacement changes of 64 μm and 52 μm, respectively, with adjustment times of 120 ms and 92 ms. The proposed control method achieved a displacement change of 38 μm, demonstrating approximately 40.6% and 26.9% lower axial displacement deviations compared to FOC and FNNIS methods. Its adjustment time was 74 ms, representing reductions of 38.3% and 19.6% relative to the comparison algorithms. Fig. 19 provides a comprehensive statistical comparison of hybrid magnetic bearings' anti-interference performance. The bar chart with error bars visually illustrates the performance differences among three control strategies. Experimental results demonstrate that the IGA-FNNIS control method exhibits superior decoupling performance.

6. CONCLUSION

The Mamdani fuzzy neural network-based decoupling control approach is introduced to tackle the nonlinear and strong coupling issues in the PMa-BSynRM. The novel approach presented in this work is theoretically analyzed and demonstrated by comparison of simulated results and experimental data, and the key points are as follows:

1. This paper analyzes the reversibility of 5-DOF-PMa-BSynRM and verifies the feasibility of the Mamdani FNN decoupling control method.

2. In view of the difficulty in parameter selection, IGA is used to optimize the number of rules and the center and width of the membership function, so as to speed up the decoupling.

3. Simulation results with 5-DOF demonstrate the dynamic decoupling capability of the IGA-FNNIS method, achieving effective decoupling among the five degrees of freedom. Furthermore, experimental results conducted using the subsystem also demonstrate the feasibility of this algorithm.

4. Since the 5-DOF experimental platform is still undergoing optimization and debugging, this study primarily utilizes subsystems for experimental validation at this stage. Future work will focus on achieving complete hardware integration and debugging of the 5-DOF system to validate the global decoupling performance of the proposed control method.

ACKNOWLEDGEMENT

This work was supported in part by the National Natural Science Foundation of China under Grants 62273168.

REFERENCES

[1] Zhu, H. and Y. Shi, "Displacement self-sensing control of permanent magnet assisted bearingless synchronous reluctance motor based on least square support vector machine optimized by improved NSGA-II," *IEEE Transactions on Industrial Electronics*, Vol. 71, No. 2, 1201–1211, Feb. 2024.

[2] Hua, Y., H. Zhu, M. Gao, and Z. Ji, "Multiobjective optimization design of permanent magnet assisted bearingless synchronous reluctance motor using NSGA-II," *IEEE Transactions on Industrial Electronics*, Vol. 68, No. 11, 10 477–10 487, Nov. 2021.

[3] Ding, H., H. Zhu, and Y. Hua, "Optimization design of bearingless synchronous reluctance motor," *IEEE Transactions on Applied Superconductivity*, Vol. 28, No. 3, 1–5, Apr. 2018.

[4] Gao, Y., D. Jiang, H. Zhu, B. Mao, and Y. Liu, "Design optimization of asymmetric permanent magnet assisted bearingless synchronous reluctance motor," *IEEE Transactions on Energy Conversion*, Vol. 40, No. 2, 1644–1654, 2025.

[5] Zhang, W., Y. Ruan, S. Ji, X. Sun, and H. Zhu, "Variable stiffness coefficient analysis and control system study for radial AC hybrid magnetic bearing," in *Proceedings of the 30th Chinese Control Conference*, 3494–3499, Yantai, China, 2011.

[6] Zhang, S. and F. L. Luo, "Direct control of radial displacement for bearingless permanent-magnet-type synchronous motors," *IEEE Transactions on Industrial Electronics*, Vol. 56, No. 2, 542–552, 2009.

[7] Bu, W., X. Zhang, and F. He, "Sliding mode variable structure control strategy of bearingless induction motor based on inverse system decoupling," *IEEJ Transactions on Electrical and Electronic Engineering*, Vol. 13, No. 7, 1052–1059, 2018.

[8] Feng, D., L. Zhu, X. Diao, and H. Zhu, "Decoupling control of bearingless synchronous reluctance motor based on support vector machines inverse system," in *Proceedings of the 32nd Chinese Control Conference*, 547–551, Xi'an, China, 2013.

[9] Zou, H., X. Diao, H. Zhu, T. Li, and D. Zhu, "Decoupling control of bearingless synchronous reluctance motor based on support vector machines inverse system," in *Proceedings of the 29th Chinese Control Conference*, 711–716, Beijing, China, Jul. 2010.

[10] Xu, B., H. Zhu, and X. Wang, "Decoupling control of outer rotor coreless bearingless permanent magnet synchronous motor based on least squares support vector machine generalized inverse optimized by improved genetic algorithm," *IEEE Transactions on Industrial Electronics*, Vol. 69, No. 12, 12 182–12 190, 2022.

[11] Zhou, J. and Z. Li, "Improved genetic algorithm to optimize BP neural network," in *2022 IEEE 10th Joint International Information Technology and Artificial Intelligence Conference (ITAIC)*, 1347–1350, Chongqing, China, Jun. 2022.

[12] Sun, X., L. Chen, H. Jiang, Z. Yang, J. Chen, and W. Zhang, "High-performance control for a bearingless permanent-magnet synchronous motor using neural network inverse scheme plus internal model controllers," *IEEE Transactions on Industrial Electronics*, Vol. 63, No. 6, 3479–3488, 2016.

[13] Zhu, H. and Z. Gu, "Active disturbance rejection control of 5-degree-of-freedom bearingless permanent magnet synchronous motor based on fuzzy neural network inverse system," *ISA Transactions*, Vol. 101, 295–308, 2020.

[14] Jiang, C., H. Zhu, and X. Wang, "Decoupling control of outer rotor coreless bearingless permanent magnet synchronous generator based on fuzzy neural network inverse system," *IEEE Transactions on Transportation Electrification*, Vol. 9, No. 3, 3908–3917, 2023.

[15] Liu, Y., X. Diao, and H. Zhu, "Dynamic decoupling control of PMa-BSynRM based on neural network inverse system optimized by enhanced chaos PSO," *IEEE Transactions on Industrial Electronics*, Vol. 72, No. 10, 9900–9910, 2025.

[16] Diao, X., G. Yang, and H. Zhu, "Decoupling control of permanent magnet assisted bearingless synchronous reluctance motor based on fuzzy neural network inverse system optimized by improved differential evolution algorithm," *IEEE Journal of Emerging and Selected Topics in Power Electronics*, Vol. 13, No. 3, 3453–3462, 2025.

[17] Ooshima, M., A. Chiba, T. Fukao, and M. A. Rahman, "Design and analysis of permanent magnet-type bearingless motors," *IEEE Transactions on Industrial Electronics*, Vol. 43, No. 2, 292–299, 1996.

[18] Zhang, W. and H. Zhu, "Improved model and experiment for AC-DC three-degree-of-freedom hybrid magnetic bearing," *IEEE Transactions on Magnetics*, Vol. 49, No. 11, 5554–5565, 2013.